MICROSCOPY RESEARCH AND TECHNIQUE 70:000–000 (2007)

# Morphological and Chemical Studies of Pathological Human and Mice Brain at the Subcellular Level: Correlation Between Light, Electron, and NanoSIMS Microscopies

CARMEN QUINTANA,[1]* TING-DI WU,[2,3] BENOIT DELATOUR,[4] MARC DHENAIN,[2,3]
JEAN LUC GUERQUIN-KERN,[2,3] AND ALAIN CROISY[2,3]
[1]*IMM-CSIC, 8 Isaac Newton, 28760 Tres Cantos, Madrid, Spain*
[2]*INSERM U759, Orsay, France*
[3]*Institut Curie Recherche, Centre Universitaire, 91405 Orsay Cedex, France*
[4]*CNRS UMR 8620, Université Paris-Sud, 91405 Orsay Cedex, France*

*KEY WORDS* neuropathology; Alzheimer; transgenic APP/PS1 mice; nanoSIMS; correlative microscopies

*ABSTRACT* Neurodegenerative diseases induce morphological and chemical alterations in well-characterized regions of the brain. Understanding their pathological processes requires the use of methods that assess both morphological and chemical alterations in the tissues. In the past, microprobe approaches such as scanning electron microscopy combined with an X-ray spectrometer, Proton induced X-ray emission, secondary ion mass spectrometry (SIMS), and laser microprobe mass analysis have been used for the study of pathological human brain with limited success. At the present, new SIMS instruments have been developed, such as the NanoSIMS-50$^{TM}$ ion microprobe, that allow the simultaneous identification of five elements with high sensitivity, at subcellular spatial resolution (about 50–100 nm with the $Cs^+$ source and about 150–200 nm with $O^-$ source). Working in scanning mode, 2D distribution of five elements (elemental maps) can be obtained, thus providing their exact colocalization. The analysis can be performed on semithin or ultrathin embedded sections. The possibility of using transmission electron microscopy and SIMS on the same ultrathin sections allows the correlation between structural and analytical observations at subcellular and ultrastructural level to be established. Our observations on pathological brain areas allow us to establish that the NanoSIMS-50 ion microprobe is a highly useful instrument for the imaging of the morphological and chemical alterations that take place in these brain areas. In the human brain our results put forward the subcellular distribution of iron–ferritin–hemosiderin in the hippocampus of Alzheimer disease patients. In the thalamus of transgenic mice, our results have shown the presence of Ca–Fe mineralized amyloid deposits. *Microsc. Res. Tech. 70:000–000, 2007.* © 2007 Wiley-Liss, Inc.

## INTRODUCTION

Neurodegenerative diseases (ND) induce morphological modifications in well-characterized regions of the brain. Such modifications can be studied with conventional microscopes such as light microscopes for observations at the histological level or electron microscopes for observations at the subcellular level. Altered levels of some chemical elemental constituents can be another important indicator of neurodegenerative processes. Such alterations can be studied with high sensitivity bulk analytical methods [for example, see (Andrasi et al., 1999; Griffiths et al., 1999; Rajan et al., 1997). However, in several cases, it is the distribution of the element within the tissues that is modified rather than its global level. Among the possible chemical element modifications, iron accumulations have been found in the affected brain areas of many neurological diseases [for reviews, see (Ke and Qian, 2003; Todorich and Connor, 2004)].

In the case of Alzheimer's disease (AD), the main cause of dementia in our countries, histological hallmarks are the accumulations of hyperphosphorylated tau protein in intraneuronal neurofibrillary tangles (NFT) and accumulations of β-amyloid protein in extracellular senile plaques (SPs). Iron has been found in NFT and SPs (Connor and Menzies, 1995; Grundke-Iqbal et al., 1990) using the classical histochemical "Perls" stain method (Nguyen-Legros et al., 1980). Perls stain has also been used to show iron accumulations in amyloid deposits (AmD) from the transgenic

---

*Correspondence to: Carmen Quintana, Instituto Microelectronica de Madrid, 8 Isaac Newton, 28760 Tres Cantos, Madrid, Spain.
E-mail: Carmen@imm.cnm.csic.es

Received 12 July 2006; accepted in revised form 17 October 2006

Abbreviations used: AmD, amyloid deposits; EDXS, electron dispersion X-ray spectroscopy; LAMMA, laser microprobe mass analysis; MRI, magnetic resonance imaging; ND, neurodegenerative diseases; NFT, neuro fibrillar tangles; PIXE, proton induced X-ray emission; ppm At, atoms of an element by $10^6$ total atoms; SEM, scanning electron microscopy; SIMS, secondary ion mass spectrometry; SPs, senile plaques; TEM, transmission electron microscopy.

Contract grant sponsor: Dirección General de Investigación; Contract grant number: BMC2002-00996; Contract grant sponsor: Ministerio de Educación, Directión General de Investigación, Spain; Contract grant number: PR2002-0261; Contract grant sponsor: Ministerio de Sanidad, Spain; Contract grant number: FIS-C03-006.

DOI 10.1002/jemt.20403

mouse model of amyloidosis (El Tannir El Tayara et al., 2006). In such models, Perls stain also showed that such accumulation is more marked in the amyloid plaques from the thalamus (Vanhoutte, G., 2005). However, histological methods are relatively nonspecific, have a relatively poor spatial resolution, and do not allow the measurement of several chemical elements at the same time.

Understanding the pathological processes involved in these ND requires using methods that assess both morphological and chemical alterations in the tissues, such as the microprobe approaches. Indeed, there are direct and unambiguous physical methods of multiple chemical element detection based on the physical processes taking place during the interaction of electrons, protons, or ions with the constituent's atoms of the observed samples. Among scanning electron microscopy (SEM) combined with X-ray spectrometer (EDXS), proton induced X-ray emission (PIXE), secondary ion mass spectrometry (SIMS), and laser microprobe mass analysis (LAMMA), the LAMMA method was the only one to show a precise localization of iron accumulation in brain of Alzheimer and Parkinson patients (Good et al., 1992a,b; Perls and Good, 1992).

At that time, despite its excellent sensitivity (about 1 ppm), the SIMS technique was not considered useful to study pathological brain due to a poor spatial resolution (about 1 μm) and because it only allowed sequential imaging acquisition. New dynamic SIMS instruments have been developed since then and current instruments (such as the CAMECA NanoSIMS-50™ ion microprobe) can simultaneously identify up to five elements at subcellular spatial resolution (about 50–100 nm with the $Cs^+$ source and about 150–200 nm with $O^-$ source) (Slodzian et al., 1992a,b). Working in scanning mode, 2D distribution of five elements (elemental maps) can be obtained, thus providing their exact colocalization. With such an approach, NanoSIMS maps can not only be easily correlated with light and electron microscopic images obtained in contiguous sections but also with electron microscopic images of the same thin section. Thanks to these technological advances, the NanoSIMS-50 instrument has the potential to provide new information on tissue alterations occurring in the course of AD (Quintana et al., 2006).

The aim of the present study was to evaluate the usefulness of the NanoSIMS-50 microscope for imaging of the morphological and chemical modifications in hippocampal regions of AD human brain and in thalamus regions of an APP/PS1 transgenic model of amyloidosis mice brain. The distribution of N, P, S, Fe, and Ca elements were recorded in senile plaques, pyramidal neurons, glial cells, and neuropili regions in the hippocampal regions of AD patients as well as in the thalamic plaques from the APP/PS1 mouse model of brain amyloidosis.

The combination of morphological and analytical information provided by NanoSIMS-50 with the information provided by light and analytical electron microscopies, allowed us to specify the subcellular composition of the pathological hallmarks of AD. For example, in the coronal region of SPs, Iron colocalizes with Sulfur, in the cytoplasm of neurons lipofuscin pigments can be identified by their high Sulfur content and in neuropili, the dystrophic myelinated axons can be identified by their phospholipid-composed sheet of myelin. Our results confirm and define the presence of Iron in glial cells (within lysosomes–siderosomes in the cytoplasm and nucleus). In the thalamus of APP/PS1 mice, the morphological and analytical data also confirmed the presence of iron, in low concentration, in the AmD. In addition we observed that some of these AmD are mineralized and they have high content in calcium.

## MATERIALS AND METHODS

### Brain Preparation

***Alzheimer Human Brain.*** Fresh-frozen fragments of the brain hippocampus were obtained at autopsy from patients affected with AD. The brains proceed from the Pitié-Salpetrière Brain Bank, Raymond Escourolle Neuropathology Department, Paris, France. The sample preparation has been described previously (Quintana et al., 2006). Briefly, the frozen fragments were thawed in the chemical fixative [4% paraformaldehyde and 1% glutaraldehyde in 0.4 M Hepes buffer (pH = 7)], cut in fragments of about 9 $mm^3$ that were fixed in the same fixative at room temperature for 12 h. Samples were dehydrated in ethanol and embedded in Lr-White resin at 60°C for 48 h.

***APP/PS1 Transgenic Mouse Samples.*** Transgenic APP/PS1 mice [Thy1 APP751 SL (Swedish mutation KM670/671NL, London mutation V717I introduced in human sequence APP751) × HMG PS1 M146L], modeling early-onset and progressive cerebral amyloid deposition, were used (Blanchard et al., 2003; Wirths et al., 2001a,b). Thalamic regions from two APP/PS1 mice that showed hypointense signal during in vivo magnetic resonance imaging (MRI) exams were processed. The first mouse (He26) was anesthetized by pentobarbital (5.5 mg/animal; Ceva Santé Animal®), and perfused, first with a saline solution, and then with a solution of 4% paraformaldehyde and 1% glutaraldehyde in phosphate buffer. Coronal sections of the brain thalamus regions (150 μm-thick) were obtained with a vibratome. The slices were cut in fragments of about 9 $mm^2$ that were dehydrated in ethanol and embedded in Lr-White resin at 60°C for 48 h between two glass slides covered with Sigmacote. The second mouse (He19) was killed by decapitation without perfusion. Its brain was fixed in 10% buffered formalin. The brain was then stored overnight in a solution of 20% glycerin and 2% dimethylsulfoxide in 0.1 M phosphate buffer for cryoprotection and freezing in liquid nitrogen-cooled freon. The brain was subsequently sectioned into 40 μm-thick coronal sections on a freezing microtome. Sections of thalamus region were thawed in the buffer, cut in fragments of about 9 $mm^2$ and processed as previously described. Some fragments were post-fixed with $O_sO_4$.

### Histochemical Staining of Amyloid Deposits and Histochemical Staining of Iron

The histochemical staining of amyloid deposits (AmD) and iron were performed on floating 40 μm-thick coronal sections obtained with the freezing microtome, in order to improve tissue penetration of reactives. AmD were labeled by standard Congo red staining [30 min in a 80% ethanol solution saturated with Congo red and sodium chloride; adapted from (Puchtler et al., 1962)]. Iron staining was performed using a protocol derived from the standard Perls-DAB method (Nguyen-Legros et al., 1980). Briefly, blockade of endogenous peroxydase activity was first done by immersion in a methanol/$H_20_2$ solution; slices were then treated with equal parts of freshly made, aqueous 2% potassium ferrocyanide and 2% hydrochloric acid for 20 min. Iron staining was finally intensified using diaminobenzidine as chromogen. After staining, slices were mounted on Superfrost plus slides (Fischer Bioblock Scientific, Ilkirch, France), dehydrated, and coverslipped for microscopic examination.

### Morphological Observations

Semithin, 1–2 μm thick, sections obtained with an ultramicrotome, deposited on glass slides and stained with toluidine blue were used to control the quality of the blocks and to locate target structures for further study. They were observed with an light microscope (Leica DM4000 B equipped with a DFC480-CCD camera). After selection of the regions of interest (ROI), contiguous semithin sections of 300–400 nm thick were directly collected on silicon plates for nanoSIMS analysis. Ultrathin sections of, 40–60 nm thick, were obtained with the same ultramicrotome and collected on uncovered copper (for ultrastructural observations) or uncovered titanium (for X-ray nano-analysis) grids. Ultrathin sections for ultrastructural observations were unstained or lightly stained with 2% uranyl acetate in water for 30–60 s. For X-ray microanalysis we used unstained sections.

Subcellular observations were performed with conventional transmission electron microscopes (CTEM) (Philips CM12, Jeol 1200 EXII). In some case the selection of the ROI for nanoSIMS analysis was performed during morphological examination using CTEM on thin sections. To allow straightforward SIMS mapping on such thin sections (about 60 nm thick), TEM copper grids covered with a thin Formvar film followed by a thin carbon layer were employed so as to combine mechanical strength with electrical conductivity and thus to prevent damage during ion bombardment.

### Analytical Studies

***Secondary Ion Mass Spectroscopy Imaging.*** SIMS examinations were carried out on a NanoSIMS-50 Ion Microprobe (CAMECA, France). The progress in analytical imaging by dynamic SIMS has been recently reviewed (Guerquin-Kern et al., 2005). Briefly, SIMS allows direct identification of chemical elements with high sensitivity and specificity and as a consequence, elemental distribution can be visualized (chemical mapping) by SIMS imaging. The NanoSIMS-50 instrument, operating in scanning mode, is equipped with a parallel detection system that allows the simultaneous acquisition of five elements which insures a perfect colocalization between images recorded, simultaneously. Although SIMS is a destructive technique, the examination of thin sections is possible because of the limited sample consumption that results from the high instrumental transmission for secondary ions and the parallel detection configuration of this instrument.

In the present study of pathological human and mice brain, images for $CN^-$, $P^-$, and $S^-$ were acquired simultaneously using the $Cs^+$ primary beam while during simultaneous detection for $Ca^+$ and $Fe^+$, the $O^-$ beam was employed. When using the $Cs^+$ beam, the intensity was around 3 pA with a probe size (68% intensity) of about 100 nm in diameter. The $O^-$ beam had an intensity of around 30 pA with a probe size of about 250 nm. All of the images were recorded with a definition of 256 pixel × 256 pixels. The typical acquisition duration was 15 ms per pixel during imaging of the negative secondary ion $^{12}C^{14}N^-$, $^{31}P^-$, and $^{32}S^-$, while an extended counting time of about 60 ms per pixel was needed for the detection of positive secondary ion species $^{40}Ca^+$ and $^{56}Fe^+$ at much lower intensity. In the latter case, the recording was done using multiframe mode (accumulation of 6 frames with 10 ms per pixel for each) in order to prevent structure deformation because of the erosion of primary ions.

Concerning the detection of iron in brain, $Fe^-$ emission using the $Cs^+$ beam (electronic affinity, EA: 0.16 eV) provides extremely low sensitivity. As an alternative, several tests have been carried out by detecting $FeO^-$ (EA: 1.5 eV) (Figs. 1a–1c) but unfortunately the sensitivity is still too low to allow imaging of Fe in brain. As Fe can be more favorably detected as $Fe^+$, imaging has been carried out using $O^-$ beam and the obtained Fe distribution is correlated with the maps recorded when using the $Cs^+$ beam (Figs. 1d–1f). Nevertheless, in conventional TEM preparations Ca, a highly diffusible element, is artifactually accumulated in nucleus heterochromatin. During the detection of $^{56}Fe^+$, mass interference of $^{40}Ca^{16}O^+$ must be prevented. The exact masses of $^{56}Fe$ and $^{40}Ca^{16}O$ are 55.93494 and 55.95750, respectively. Therefore, a mass resolution power of $M/\Delta M > 2479$ is required. All the procedures in the present study have been carried out under these very strict conditions. Figure 1g shows a high resolution SIMS mass spectrum of a glial cell in AD recorded at 56 amu.

Prior to imaging of iron distribution in hippocampal tissue, the detection sensitivity for Fe using the $O^-$ beam was evaluated on a test sample (Figs. 1h and 1i). We used human liver ferritin (Ft) (about 12-nm in diameter), sprayed on a carbon film where each Ft core contains a maximum number of 4,500–5,000 atoms of iron, i.e., a local iron atom density of about 5 atoms per $nm^3$. In our experimental conditions (intensity of 6-pA over a counting time of 15-ms), a mean level of 130 counts per pixel was obtained. This measured signal suggested a sensitivity of 2.8 E-3 (one detected count for 357 Fe atoms within a sputtered volume of 65 $nm^3$).

Sections were first examined using the $O^-$ beam to record $^{40}Ca^+$ and $^{56}Fe^+$ maps. The same ROI were then analyzed using the $Cs^+$ beam to acquire $^{12}C^{14}N^-$, $^{31}P^-$, and $^{32}S^-$ images in a separate run. As the two sets of images were recorded sequentially, care has been taken so as to minimize shift between the two sets of images during image acquisition. Furthermore, image processing using ImageJ software (Rasband, 1997–2006, http://rsb.info.nih.gov/ij/), with a homemade plug-in was performed to obtain proper colocalization of the observed structures on the processed maps for all of the ion species.

These processed elemental maps allow further correlation either with optical images or with high resolution TEM morphological images obtained during the selection of the ROI.

***Microprobe Analysis.*** Energy dispersion X-ray spectroscopy (EDXS) was performed with two analyti-

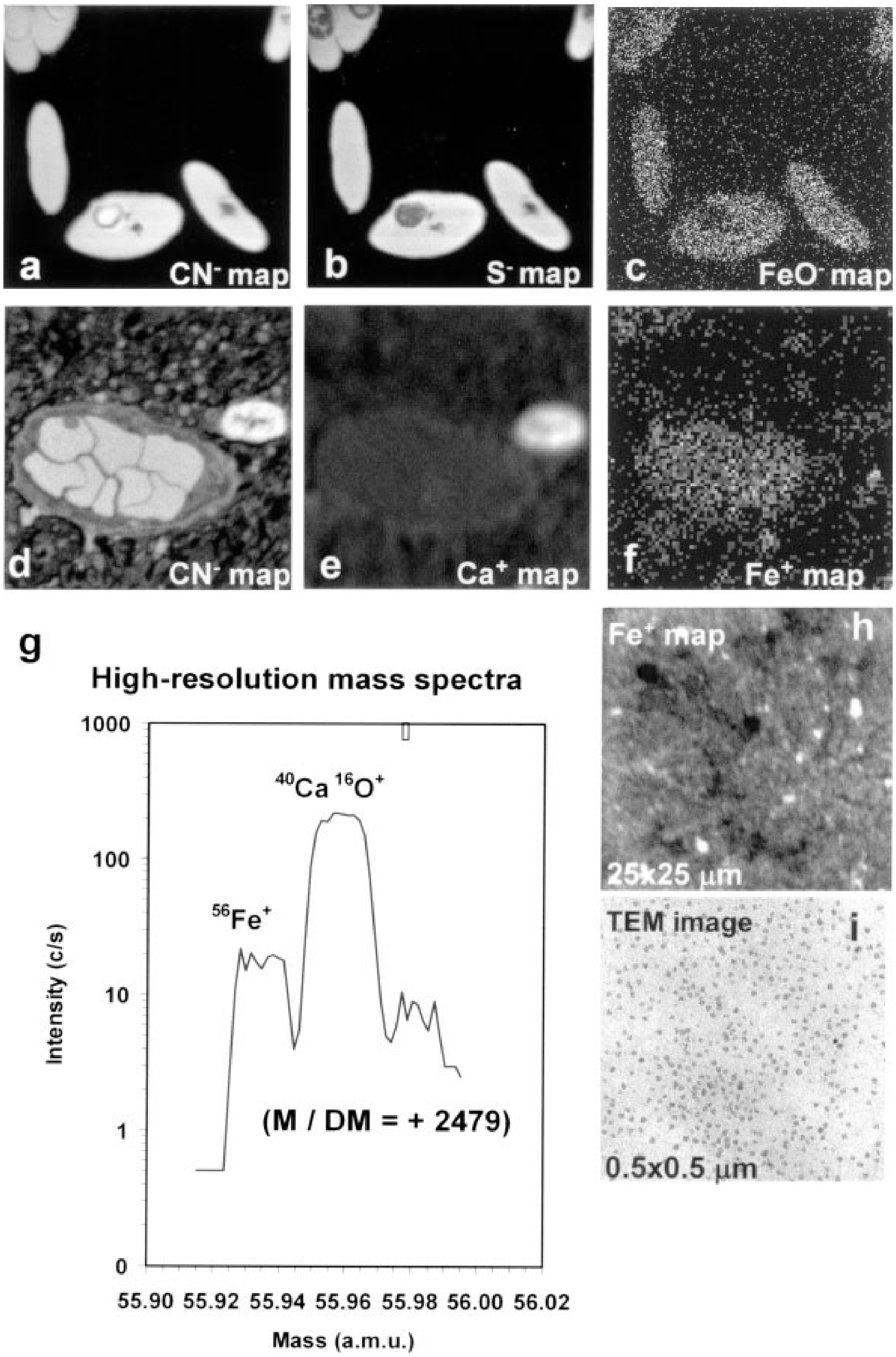

Fig. 1. Test for iron detection. (**a–c**) $CN^-$, $S^-$, and $FeO^-$ nanoSIMS maps of sectioned quail erythrocytes; (**d–f**) $CN^-$, $Ca^+$, and $Fe^+$ maps of a blood vessels containing erythrocytes in a thalamic region of transgenic mice; set of maps (a–c) corresponds to an area of 15 µm × 15 µm; set of maps (d–f) corresponds to an area of 20 µm × 20 µm; (**g**) High resolution mass spectrum at mass 56; (**h–i**) $Fe^+$ maps (20 µm × 20 µm) and close-up TEM image (0.5 µm × 0.5 µm) of analyzed sprayed ferritin molecules; the density of the ferritin molecules varies from one area to another which results in the contrast observed in the $Fe^+$ maps: the higher the ferritin density, the higher the $Fe^+$ emission. Moreover, TEM examination also shows regions free of ferritin molecules that may correspond to black areas in $Fe^+$ maps.

cal transmission electron microscopes, Philips CM12-LaB6 source, working at 120 kV and Philips CM20-FEG source, working at 200 kV.

## RESULTS

### Hippocampus of Human Alzheimer's Disease Patients

Figure 2 shows a typical optical image of a fragment of the subiculum region of the hippocampus where neurons (arrows), glial cells (arrowhead), blood vessel (bv), and some SPs (red arrows) can be observed. In Figure 3 we present two sets of images: one set of a SPs-containing region and one set of a neurons-containing region. Figures 3a and 3e are optical images and Figures 3b–3d; 3f–3g are NanoSIMS elemental maps performed on unstained 350 nm thick contiguous sections. The nanoSIMS maps correspond to the polyatomic species $CN^-$ (Fig. 3b) and the monoatomic $P^-$ (Figs. 3c and

3f) and $S^-$ species (Figs. 3d and 3g). The analyzed surfaces are 20 μm × 20 μm and 50 μm × 50 μm, respectively (figure legends).

$CN^-$ maps reveal the tissue structure with morphological details; the SPs and the surrounding structures. In particular, neuron and glial cells are well visualized with higher spatial resolution than in the optical stained images. The $P^-$ maps show the distribution of the P-containing molecules (nucleic acids, phosphorylated-proteins, and phospholipids). Regarding the distribution of nucleic acids, an important difference in the chromatin density between the nuclei of neurons and those of glial and epithelial cells can be observed. Other P-rich structures can be observed, such as punctuate P-rich structures in the cytoplasm of neurons and ring-like P-rich structures in the neuropili. The $S^-$ maps represent mainly the distribution of S-containing proteins. Senile plaques and the surrounding structures present a similar $S^-$ emission. Moreover, some S-rich structures can also be observed: granular structures near to the core of SPs (red arrow in Fig. 3d) and smaller granular structures in the cytoplasm of neurons (red arrow in Fig. 3g).

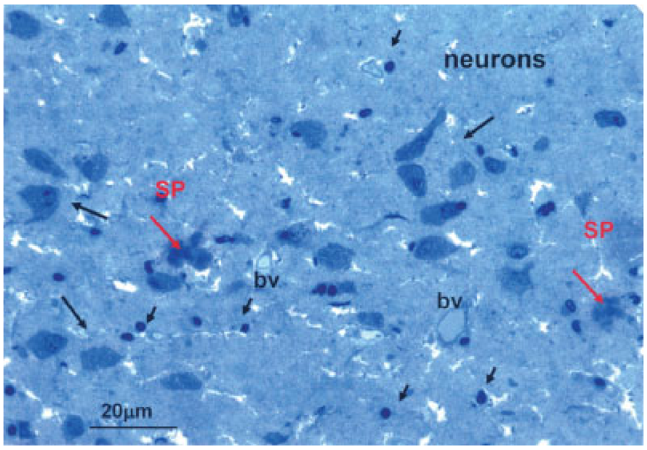

Fig. 2. Optical image of toluidine blue stained semithin resin embedded section of an AD hippocampal region; pyramidal neuron (long arrows), glial cells (arrowhead), empty blood vessels (bv), and two senile plaques (red arrows) can be observed.

Identification of S-rich and P-rich structures was made with the help of the optical fluorescence microscope and the TEM microscope (Figs. 3–5). The S-rich granular structures present in the cytoplasm of neurons (Fig. 3g) have been identified as lipofuscin granules from their natural fluorescence emission between 570 and 750 nm. In Figure 3h we show a phase contrast optical image (pink) superposed to the natural fluorescence image (yellow) performed on unstained semithin sections of the pyramidal neurons-containing regions. Morphological examination by TEM was necessary for the identification of the S-rich structures near the senile plaques. For this purpose, a series of nanoSIMS analyses have been performed on thin sections previously observed by TEM. Figures 4a–4e show low magnification TEM images and nanoSIMS $CN^-$ and $S^-$ maps of the same SP containing region on the same thin section. At higher TEM magnification (Figs. 5f and 5g) it is possible to identify these structures as dystrophic neurites (DN), one component of senile plaques.

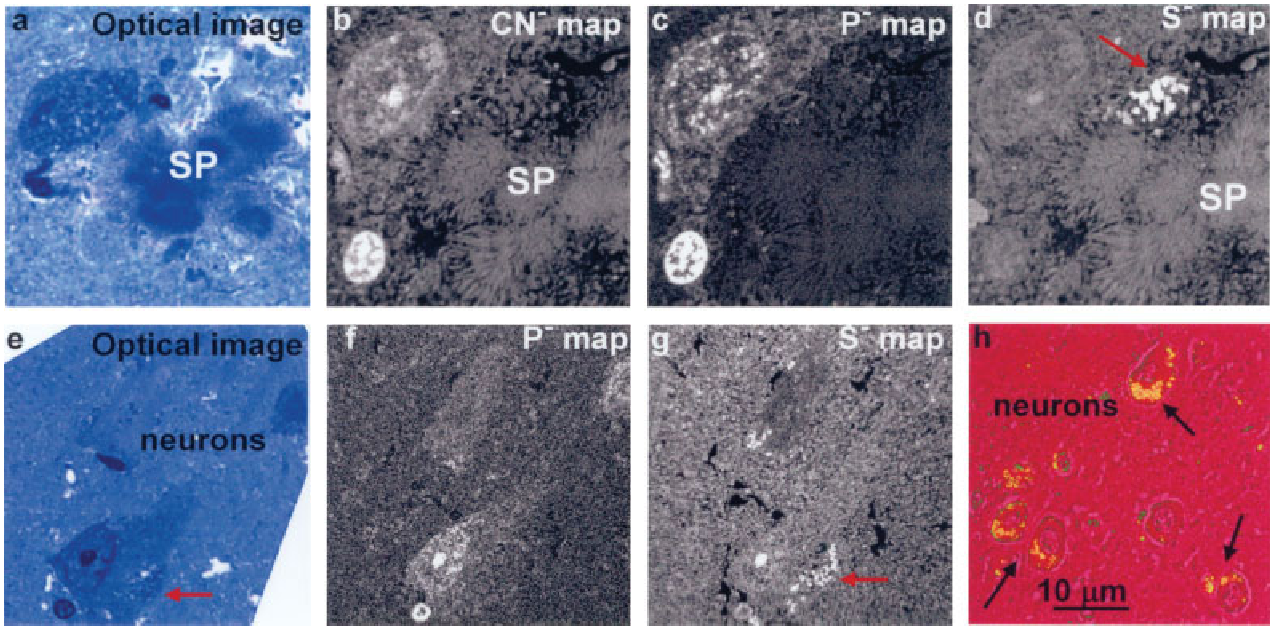

Fig. 3. Optical images and nanoSIMS maps recorded on two adjacent semithin sections; (**a**–**d**) one of a SPs-containing region and one (**e**–**h**) of a pyramidal neurons-containing region. (**a** and **e**) optical images performed on toluidine blue-stained sections, (**b**) $CN^-$ map, (**c** and **f**) $P^-$ maps, and (**d** and **g**) $S^-$ maps where areas with high emission can be observed around of SPs (d) and in the cytoplasm of neurons (**g**). Set of maps (**b**–**d**) corresponds to an area of 20 μm × 20 μm, set of maps (**f** and **g**) corresponds to an area of 50 μm × 50 μm. The intraneuronal S-rich structures have been identified as lipofuscin granules due to their natural fluorescence emission: (**h**) optical phase contrast image of a set of pyramidal neurons (pink) superposed onto the fluorescence image where the natural fluorescence emission of cytoplasmic lipofuscin granules (yellow) can be observed; images performed on unstained sections.

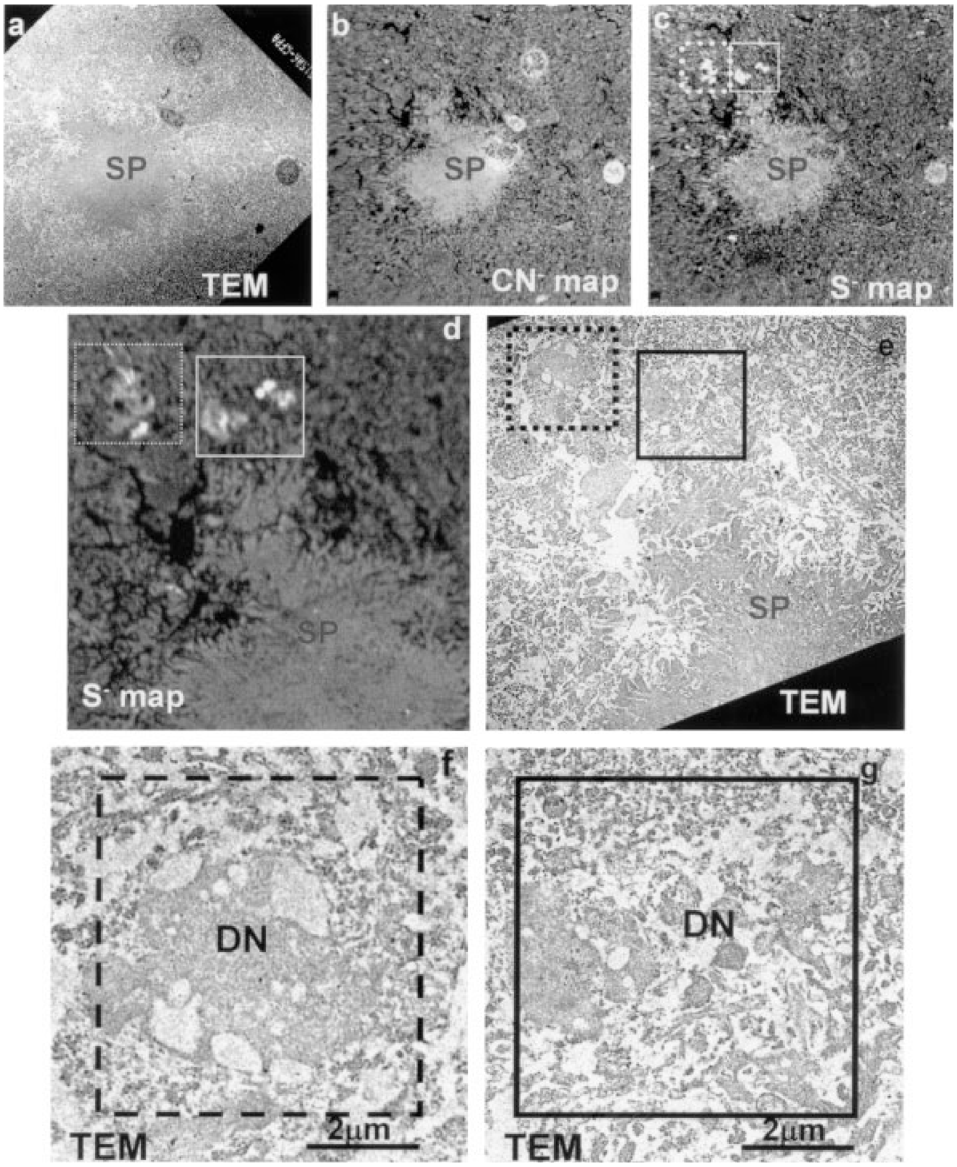

Fig. 4. Identification of S-rich structures in the periphery of senile plaques as dystrophic neurites. (**a**, **e**, **f**, and **g**) TEM images, (**b–d**) CN$^-$ and S$^-$ nanoSIMS maps at different magnifications. (**a–c**) [area of 50 μm × 50 μm]; (**d–e**) [area of 25 μm × 25 μm]. (**f** and **g**) detail of inset regions of (**e**) [area of 8 μm × 8 μm].

In the same manner we have identified the punctuate P-rich structures in the cytoplasm of neurons as endoplasmic reticulum and intraneuronal NFT (long arrows in Figs. 5a and 5b). Images of P-rich ring-like structures observed in neuropili have been illustrated in Figures 5a–5c (short arrows). These structures have been imaged by TEM in unstained thin sections prior to nanoSIMS analysis. Figure 5c shows the P$^-$ map of a neuron and adjacent neuropili region where P$^-$ rich ring-like structures are noted as Figs. 1, 2, 3. Figures 5d–5f represent details of the P$^-$ map of these structures noted as Figs. 1, 2, 3, and Figures 5d′–5f′ represent the TEM images at similar magnification. In Figures 5g and 5h we presented TEM images at higher magnification of this type of structures that allows them to be identified as myelinated axons; the P-rich ring-like structures correspond to myelin sheets which are mainly composed of phospholipids.

As iron can be more favorably detected as Fe$^+$, imaging has been carried out using the O$^-$ beam and the obtained Fe distribution is correlated with the maps recorded by using the Cs$^+$ beam. The iron maps show that no detectable signal was observed in the central region of SPs; iron is present in the S-rich structure in the periphery of SPs (Figs. 6a and 6b), identified as DN. Iron is also observed in glial cells (Fig. 6e). Figure 6f show the superposed P$^-$ (in green) and Fe$^+$ (in red) maps. It can be observed that in some glial cells (encircled areas) iron is also present in the nucleus. The punctuate regions in the cytoplasm of glial cells (arrowhead) correspond to lysosomes-siderosomes containing ferritin (Ft)–hemosiderin (Hm) molecules (Quintana et al., 2006). The S-rich lipofuscin granules in cytoplasm of neurons do not contain iron.

## Thalamus of Transgenic APP/PS1 Mice

In vivo and postmortem MRI observation of transgenic APP/PS1 mice reported the occurrence of hypointense spots in thalamic areas (Vanhoutte et al., 2005). Histochemical studies performed on 40 μm thick coronal tha-

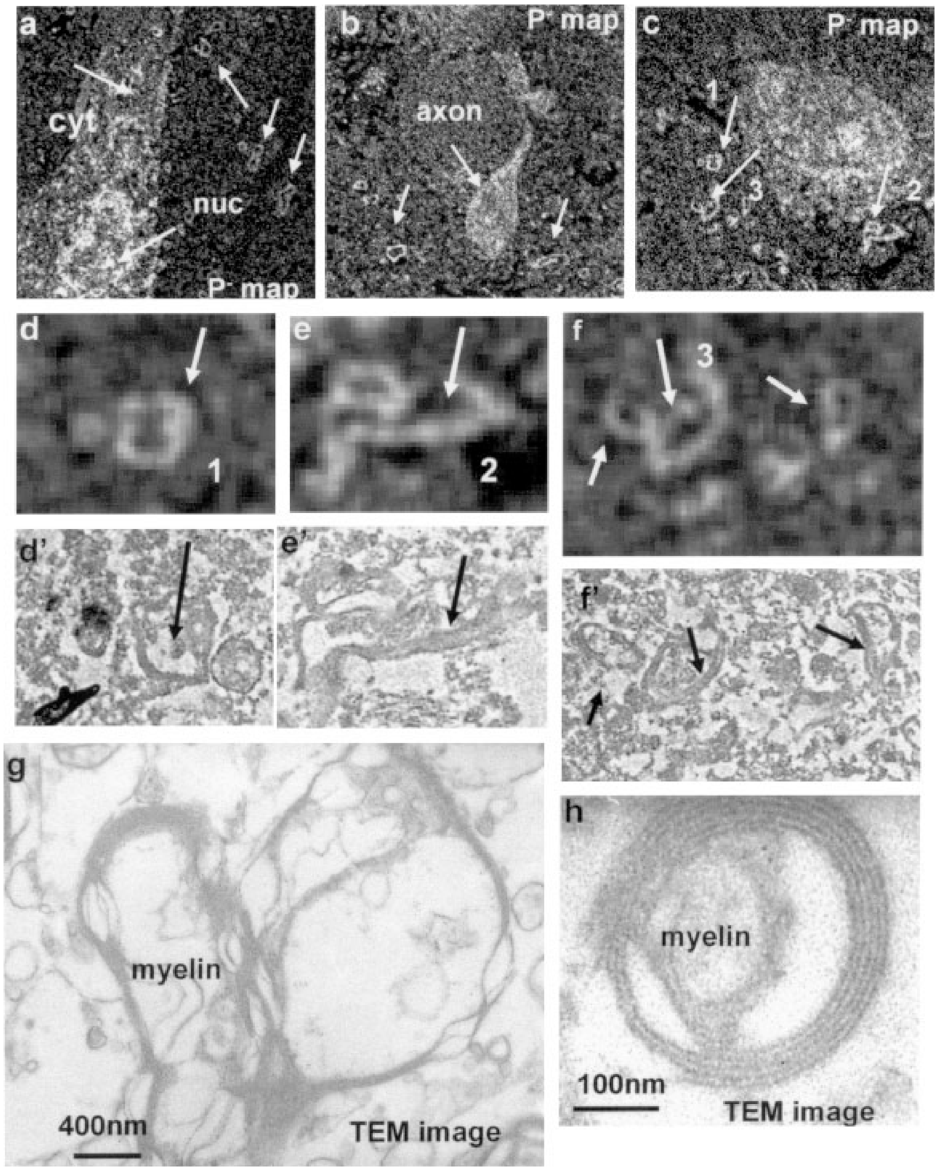

Fig. 5. Identification of ring-like P-rich structures as myelinated axons; (**a–c**) $P^-$ nanoSIMS maps of neuron containing regions where ring-like P-rich structures can be observed in the adjacent neuropili; analyzed area of 20 μm × 20 μm, 18 μm × 18 μm, and 20 μm × 19.2 μm, respectively; (**d–f**) detail of regions labeled 1, 2, 3 (arrows) in (**c**) with the corresponding TEM images at the same magnification (**d′–f′**); (**g** and **h**) TEM images at higher magnification showing the sheet of phospholipids contained myelin in axons.

lamic cryosections (Dhenain et al., Characterization of in vivo MRI detectable thalamic plaques from APP/PS1 mice, manuscript in preparation; El Tannir El Tayara et al., 2006), show that such spots colocalize with AmD and iron. One example is shown in Figures 7a–7c.

Further histological observation of the morphology of the thalamus was performed on toluidine blue 1–2 μm semithin stained sections. Figure 7d shows an optical image of the thalamus corresponding to the first protocol of brain preparation (see material and methods). Neurons, glial cells, blood vessel (empty in this first protocol), and AmD can be observed. Two types of AmD were observed: βA-I with homogenous toluidine blue staining (red arrows) and βA- II (black arrows) with heavily toluidine blue-stained regions. In addition to well identified AmD, dense brown bodies (that we called "aggregates") of different sizes (5–100 μm) were observed (arrowhead).

At the subcellular level, the morphology of the AmD and the "aggregates" were studied by TEM either on unstained thin sections or on thin sections lightly stained with uranyl acetate. The morphology of βA-I corresponds to the classical description of the AmD composed of bundles of compact β-Amyloid protein fibers (x), (Fig. 8a).The βA-II, displaying higher toluidine blue stained regions in optical images, had a different morphology than βA-I (Fig. 8b); regions situated in the center or/and in the edges of these deposits (+) had a different and smoother texture than the amyloid regions that appear as bundles of compact fibers (×). Immunogold assays with βA4G8 antibody show that these regions of "smooth" texture do not label with the βA antibody (results not shown, Dhenain et al., Characterization of in vivo MRI detectable thalamic plaques from APP/PS1 mice, manuscript in preparation).

The "aggregates" have an electron-dense structure (Fig. 8c), some of them show concentric layers and they are surrounded by fibers of βA protein. X-ray electron probe microanalysis performed on these aggregates show a high concentration of Ca and P while Fe is not

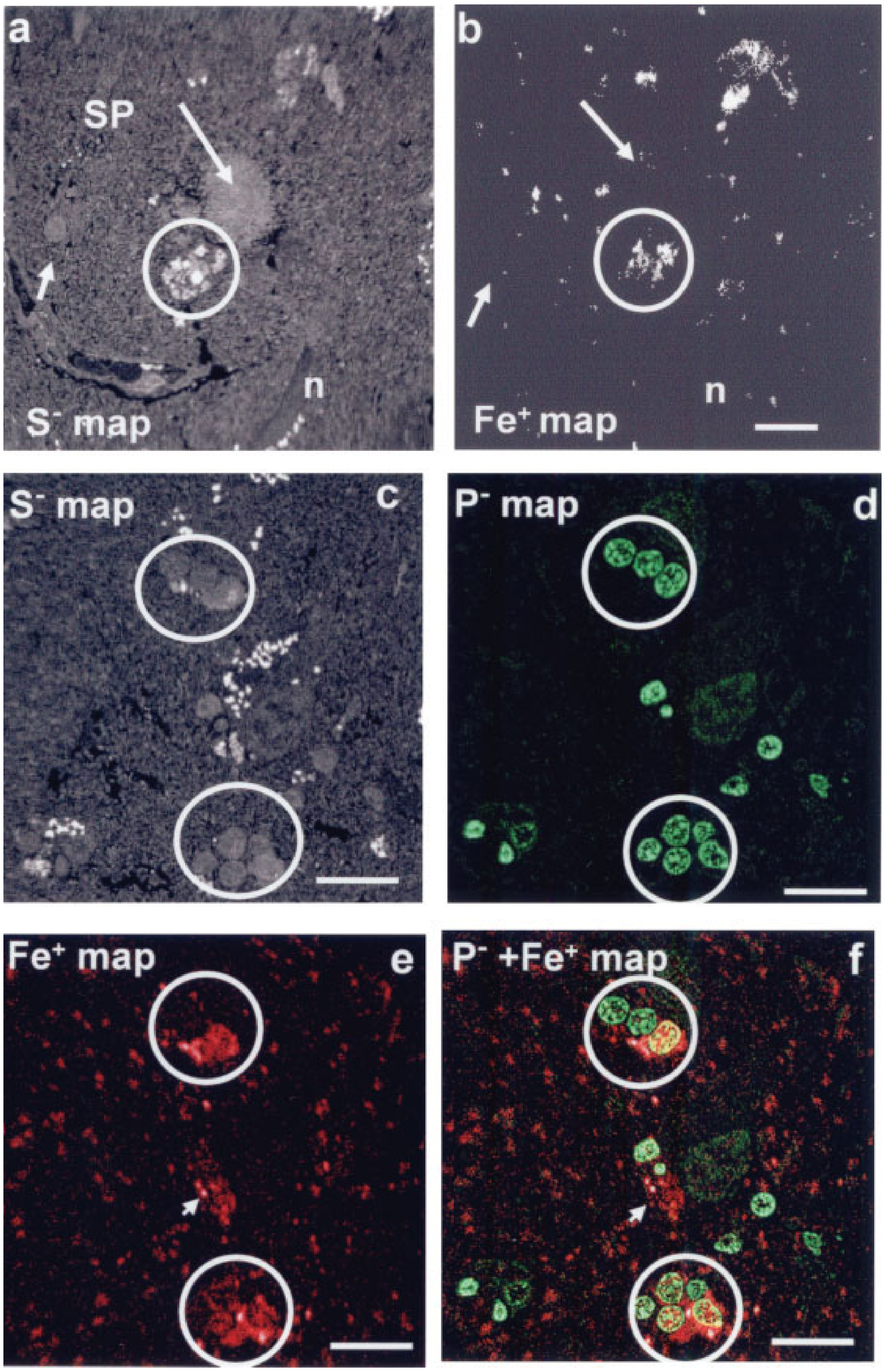

Fig. 6. Iron distribution in an hippocampal region of AD; (**a** and **b**) S$^-$ and Fe$^+$ maps of a senile plaque containing region showing the presence of iron in dystrophic neurites, iron is not detected in the core of SP; (**c**–**e**) S$^-$, P$^-$, and Fe$^+$ maps of a region containing a set of glial cells and neurons with lipofuscin granules. (**f**) digital superposition of P$^-$ and Fe$^+$ maps showing the presence of iron in the cytoplasm and nucleus of glial cells. Scale 10 μm.

significantly detected (Fig. 8d). Electron diffraction patterns show a polycrystalline structure mainly in the edge (Fig. 9a). The measured interplanar spacing (0.34, 0.28, 0.23, 0.19, 0.18, 0.17, 0.14, and 0.13 nm) appears to be similar to that of hydroxyapatite (HA) and octacalcium phosphate, the two calcium phosphates principally found in biomineralizations (Suvorova and Buffat, 2001).

NanoSIMS analysis of the "aggregates" has been performed on the same section previously observed in TEM (Fig. 9b). TEM and elemental maps for O$^-$, CN$^-$, S$^-$, and P$^-$ recorded, simultaneously are shown in Figures 9d–9g. An additional CaO$^-$ map was recorded and is shown in Figure 9h. However, at mass 72, no detectable signal of the polyatomic species $^{72}$FeO$^-$ was obtained with the Cs$^+$ beam. Figure 10a show a TEM image of two βA-II with "smooth" edges similar to those shown in Figure 8b together with the corresponding NanoSIMS maps for CN$^-$ and S$^-$ performed on an adjacent section. A blood vessel with erythrocytes (arrow) can be observed near the smaller βA-II. On the same region of the same section, Ca and Fe have been

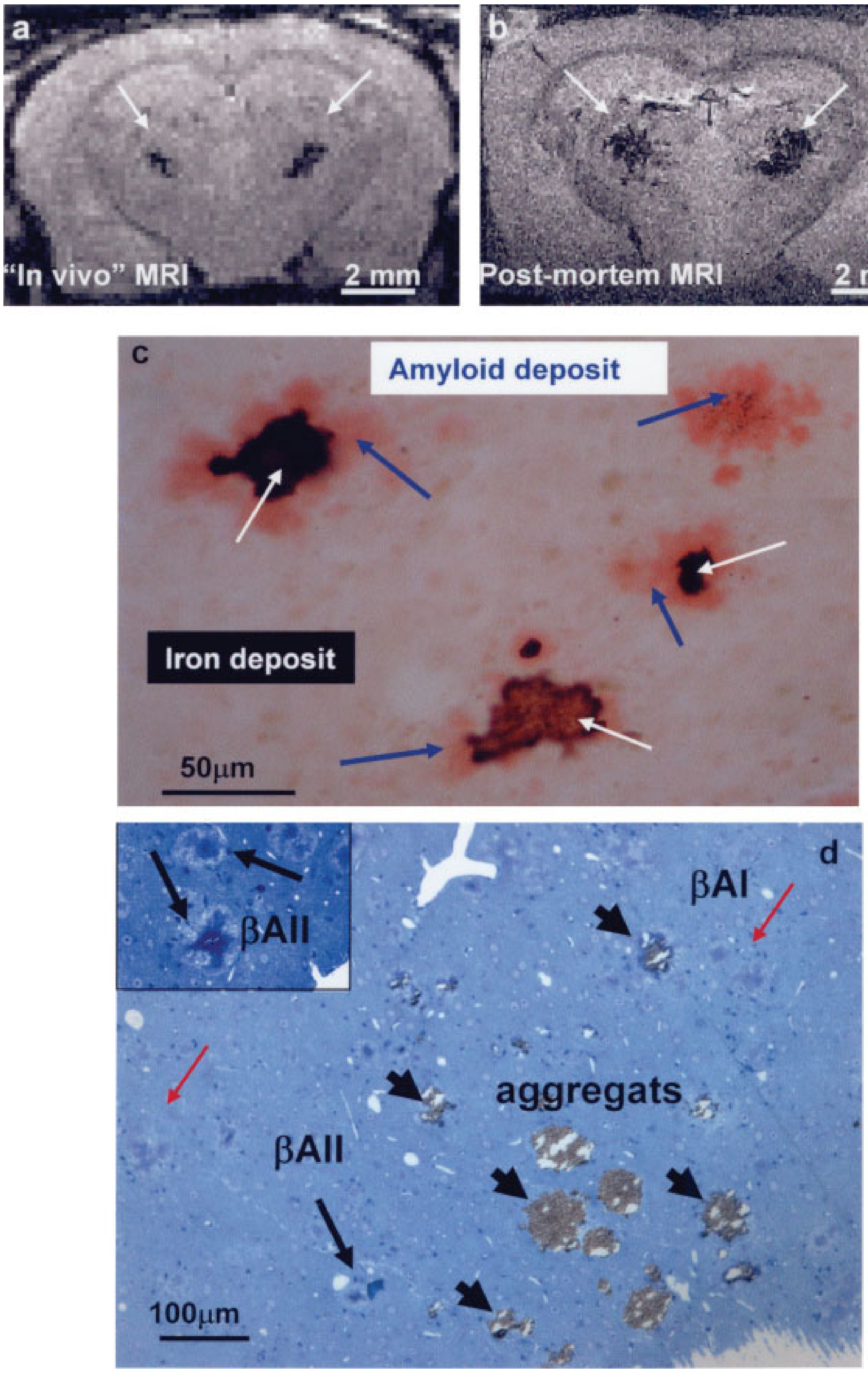

Fig. 7. APP/ PS1 transgenic mice. (**a** and **b**) "In vivo" and post-mortem magnetic resonance images (MRI) of the thalamic region of the mice studied by microanalysis showing the hipointense spots (long white arrows); (**c**) histological cryosection of the same region, double Perls and red-congo staining, brown zones correspond to Perls (iron) positive staining and red zones to β-amyloid positive staining; (**d**) optical image of a toluidine blue stained semithin resin embedded section of a APP/ PS1 transgenic thalamic region. According to the staining intensity, two types of amyloid deposits are observed; deposits with homogeneous staining (βA-I), (red arrows) and deposits with heterogeneous staining (βA-II), (long arrows). We also observed dense "aggregates" (arrowhead).

mapped as $^{40}Ca^{+}$ and $^{56}Fe^{+}$ using the $O^{-}$ beam in a separate acquisition (Figs. 10d and 10e). The nanoSIMS maps show that βA-II are proteinaceous Ca and Fe-rich structures. It can be observed that the $Fe^{+}$ emission of the amyloid deposit is lower than the $Fe^{+}$ emission of the neighboring erythrocytes (hemoglobin contains 4 atoms of Fe by molecule). Again, X-Ray microanalysis has been performed to confirm these results. Figures 10f and 10g show the X-Ray spectra obtained on the erythrocytes and on the amyloid deposit: the Fe/S concentration in βA-II is about 40% lower than in erythrocytes as it is shown in an X-ray Cliff-Lorimer standardless semiquantitative analysis (Table 1).

## DISCUSSION

In the nineties, multipoint microprobe X-ray and laser mass (LAMMA) analysis were used for the study of pathological human brain. The presence of Iron (and aluminum) was reported in neuromelanin-containing

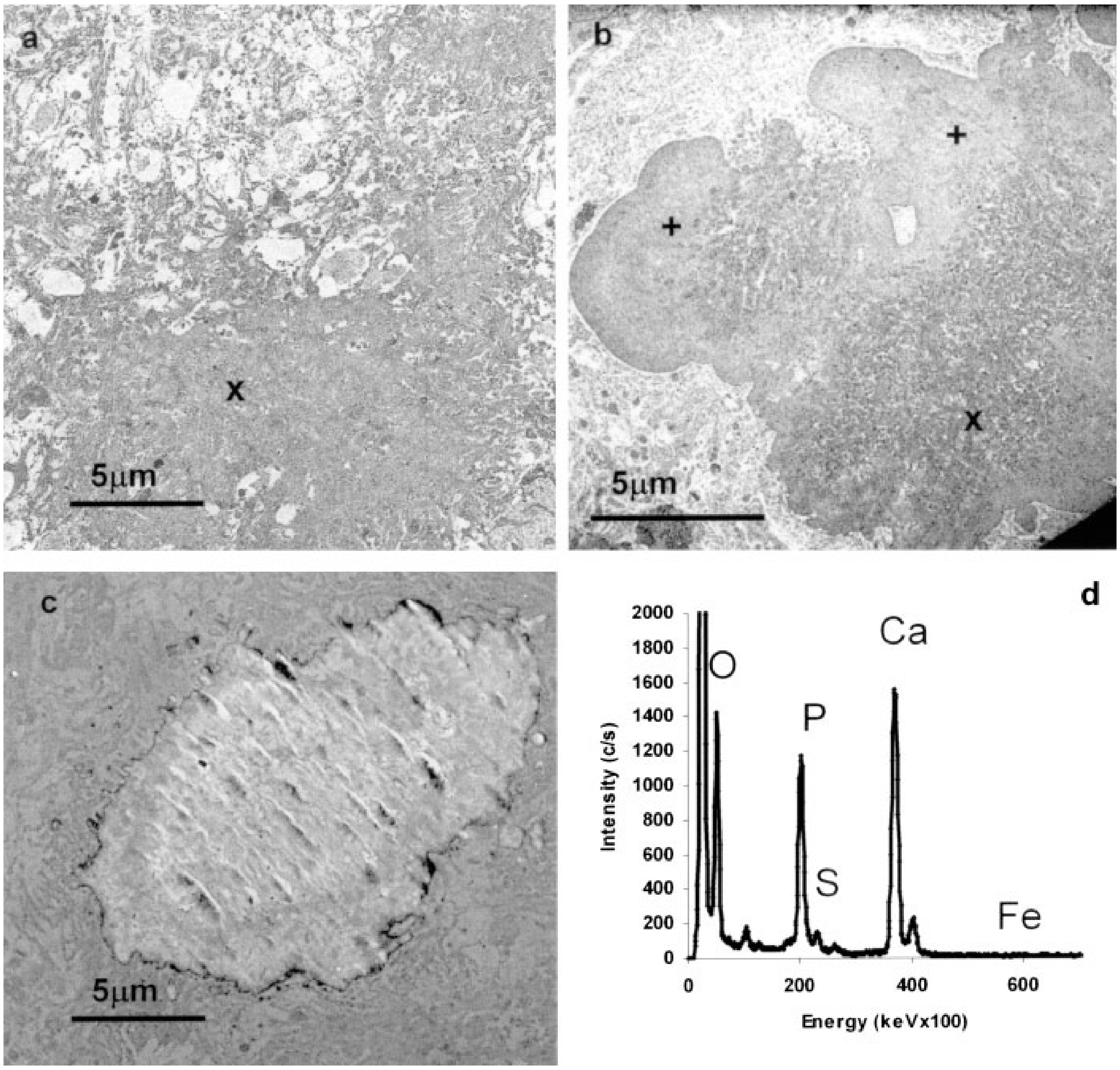

Fig. 8. TEM images of amyloid deposits. (**a**) classical amyloid deposits, βA-I, composed of bundles of fibers of β-amyloid protein (x), (**b**) Morphology of βA-II; areas composed of bundles of compact fibers of β-amyloid protein (x) coexist in the same deposits with smooth regions (+); (**c**) morphology of the "aggregates," an electron-dense structure; some of them showing concentric layers. (**d**) X-ray spectra of "aggregates" showing a high concentration for Ca and P while Fe is not significantly detected.

neurons (Good et al., 1992b; Jellinger et al., 1992), in Lewy bodies (Hirsch et al., 1991) of the substantia nigra in Parkinson patients and in NFT of AD (Good et al., 1992a).

At the present time, NanoSIMS microscopy allows the visualization of the morphological and chemical alterations taking place in well-characterized regions of pathological brain at subcellular level. Currently nanoSIMS analysis of biological samples is mainly performed on semithin sections of resin-embedded tissue placed on a conductive support. However, because of the low rate of pulverization, nanoSIMS analysis can also be performed on ultrathin resin embedded sections deposed on TEM grids covered with a conductive support such as a carbon film. Consequently, correlation between structural and analytical observations can be performed at subcellular and at ultrastructural level. Together with TEM observations at high magnifications and/or immunogold analysis of the ROI these correlations can lead to new physiological and pathological information.

In NanoSIMS microscopy, the cellular and subcellular morphology can be directly visualized in the $CN^-$ maps on unstained sections that mainly reveal the differences in Nitrogen between proteins and nucleic acids.[1] That is, because the polyatomic $CN^-$ species is mostly formed by the combination of sputtered C and N secondary particles and the C concentration is almost the same for both type of molecules (29% At in pure molecules or 40% in embedded tissues). Comparison between $CN^-$ maps with bright field TEM images

---

[1] N concentration is about 8%At in pure proteins and 11%At in pure nucleic acids, respectively; that correspond to about 2.4%At and 4.4%At in cytoplasm (70% of water) and nucleus (60% of water) of cells in embedded tissues (Leapman and Ornberg, 1988; Von Zglinicki and Bimmler, 1987).

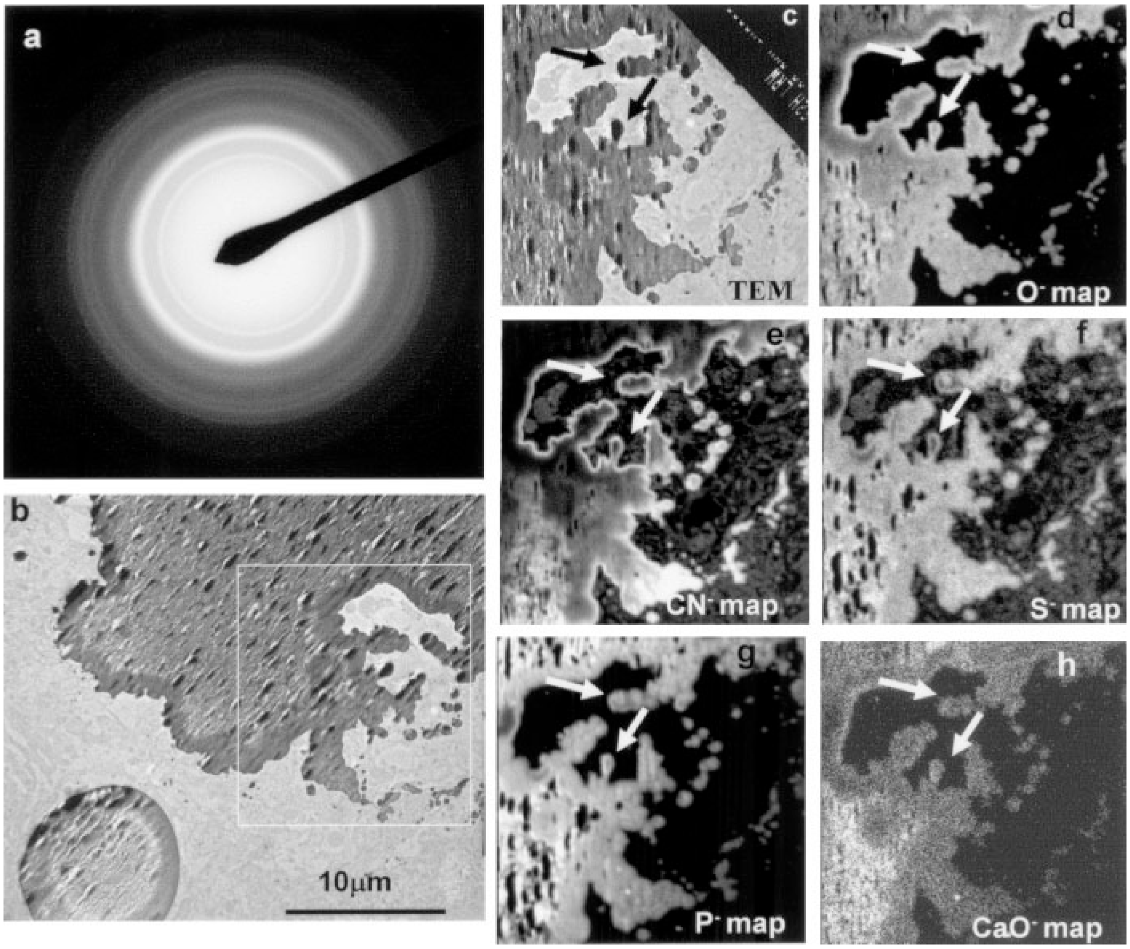

Fig. 9. TEM images of amyloid deposits. (**a**) selected area of electron diffraction of "aggregates" showing polycrystalline structure mainly in the edge; (**b–h**) TEM and nanoSIMS images of the same region of an "aggregate"; (**b** and **c**) TEM images; (**d–h**) nanoSIMS maps showing the distribution of $O^-$, $CN^-$, $S^-$, $P^-$, and $CaO^-$ in the aggregate; [area of 15 μm × 15 μm].

of the same region, performed on the same thin unstained sections, show similar and reverse contrast (Figs. 4a and 4b), i.e., mass thickness ($\rho t$) contrast. Considering that the analyzed thickness, $t$, is only a few monolayers, it can be considered that the contrast of $CN^-$ maps also correspond to the differences in the local density, $\rho$ (the protein density is 1.2–1.4 g/cc and the DNA–RNA density is 1.6 g/cc.).

Thank to the high concentration of P in nucleic acid (3% At in pure DNA–RNA, about 1.2% At in embedded tissues) and the very low or null concentration of P in proteins, the nuclei of cells are the structures better visualized in $P^-$ maps; differences in physiological and/or pathological state of nuclei can be consequently studied in $P^-$ maps. Proteins contain S in a mean concentration of 0.2% At (about 0.06% At in embedded cytoplasm). The $S^-$ maps of biological tissues sections present, in general, a low and homogeneous emission. On the other hand, the high sensitivity and subcellular spatial resolution of nanoSIMS maps allows the identification of P and S rich structures in the analyzed regions that do not correspond to nucleic acids or S containing proteins

Pathological chemical alterations linked to morphological modifications can be directly visualized by simultaneous recording of $CN^-$ maps and the maps of specific biological elements, such as $P^-$ and $S^-$. In some pathology, such as those we have studied, accumulations of some natural elements such as iron and calcium are found, that can be visualized in the simultaneous recorded $FeO^-$ and $CaO^-$ maps or in the sequential recorded $Fe^+$ and $Ca^+$ maps.

In the hippocampal region of AD patients, senile plaques, one of the main hallmarks of Alzheimer disease, are visualized, with better resolution than in optical images, in $CN^-$ and $S^-$ maps as a dense protein core and a coronal region formed of bundles of fibers. Neurons, glial cells, and dystriphic neurites can be observed around these structures. S has been found (associated to Fe) in the periphery of SPs in granular structures identified as DN containing sulfated proteoglycans (Young et al., 1989). Lypofuscin, a cytoplasmic pigment related to cell aging and pathology can be visualized by their high S concentration. Neurons and glial cells can also be distinguished in $CN^-$ and $P^-$ maps; great differences in the state of chromatin con-

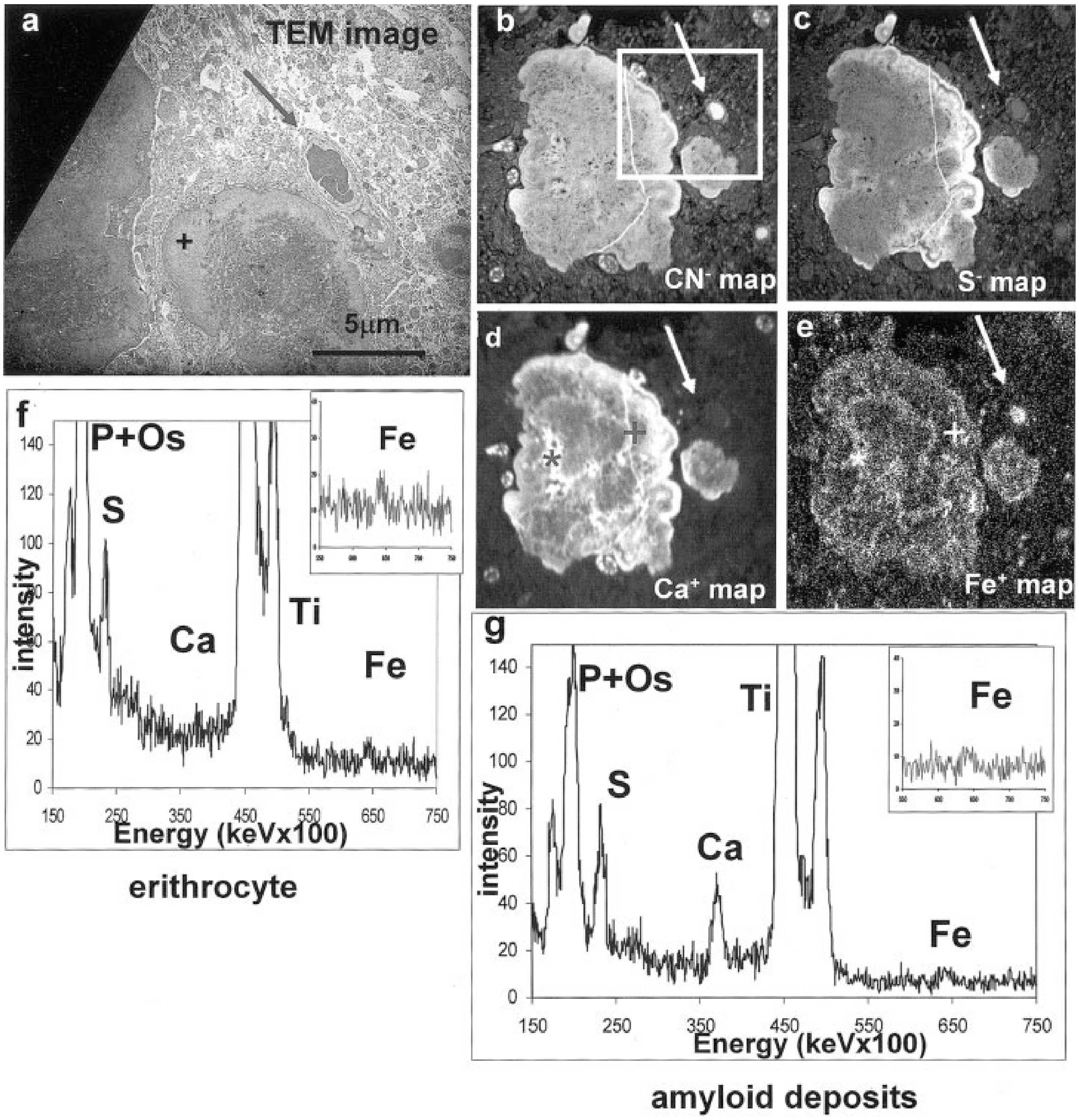

Fig. 10. (**a**) TEM image and (**b–e**) $CN^-$, $S^-$, $Ca^+$, and $Fe^+$ maps of a region containing two βA-II and one near blood vessel containing erythrocytes, used as reference for iron (arrow); analyzed area of 50 μm × 50 μm; (**f** and **g**) X-ray spectra recorded on erythrocytes and the amyloid deposits respectively; compared with the X-ray spectra of "aggregates" (Fig. 8d): the βA-II shows the presence of iron and a lower degree of calcification. Ti peak comes from the grid.

*TABLE 1. Semiquantitative X-ray microanalysis (Cliff-Lorimer standard-less method)*

| | S | Ca | Fe | Fe/S |
|---|---|---|---|---|
| Erythrocyte | 76 + 7 | 11 | 13 + 1 | 0.17 + 0.3 |
| Amyloid deposits | 69 + 7 | 24 | 7 + 1 | 0.10 + 0.02 |

densation can be observed in the nuclei of neurons and glial cells. The intraneuronal neurofibrilar tangles (NFT) composed of bundles of hyperphosphorylated tau protein are responsible for the high $P^-$ emission in cytoplasm and axonal extension of neurons. In the neuropili, the high $P^-$ emission of the myelin sheet, composed of phospholipids, allows the visualization of the dystrophic myelinated axons, which are not observable in optical images.

Iron can be mapped with the polyatomic species $FeO^-$ in the same acquisition that $CN^-$ and $P^-$ (or $S^-$) maps in erythrocytes, but unfortunately the sensitivity is too low to allow imaging of iron in the brain. Fe distribution was observed by detecting sputtered secondary positive ions, $Fe^+$, using the primary $O^-$ beam, in a separate acquisition and with a lower spatial resolution. The detection sensitivity for Fe using $O^-$ beam was evaluated on Ft molecules, and estimated to about $2.8 \times 10^{-3}$, under our experimental conditions (see earlier, Materials and methods, part secondary ion mass spectroscopy imaging). $Fe^+$ distribution was correlated with the negative ion maps recorded using the primary $Cs^+$ beam on the same ROI. Direct and precise superposition of $Fe^+$ map with $CN^-$, $P^-$, and $S^-$ maps cannot be done because of the following reasons: (1) the possible shift in beam pointing, (2) different spatial resolution of maps, and (3) difference in size and orientation or/and distortion of maps. In our case Ca accumulation in cell nuclei observed in $Ca^+$ maps (preparative artifact), has been served as a reference to correct the shift between the positive and negative maps.

In this way it has been observed that iron is detected at the periphery of SPs but not in the dense core (Connor and Mezies, 1995; Grundke-Iqbal et al., 1990). We do not observe iron associated with NFT's as was previously observed by histochemistry (Smith et al., 1997) or LAMMA (Good et al., 1992a). Our observations confirm the histochemical observations regarding the presence of iron in glial cells. Moreover, with higher spatial resolution, $Fe^+$ maps show that iron is present in the nucleus and in punctuates regions within the cytoplasm of the cells. TEM observation at higher magnification of the analyzed ROI, SPs, neurons, glial cells and neuropili, shows that all iron-rich regions mapped by nanoSIMS coincide with the Ft or Hm rich regions (Quintana et al., 2006). At this time, we can affirm that the punctuate Fe-rich regions in the cytoplasm of glial cells are lysosomes and/or siderosomes containing Ft and Hm.

In the thalamus region in APP/PS1 mice, histological observations of toluidine blue stained 1–2 μm semithin resin embedded sections showed, with better resolution that in histological observations on nonembedded 40 μm thick frozen sections, the morphological heterogeneity of AmD (the equivalent of senile plaques in human AD brain). Further, NanoSims analysis showed that these AmD present high emissions of $CN^-$ and $S^-$ ions, in agreement with their protein composition. Furthermore, some of the AmD present high $Ca^+$ emission corresponding to different degrees of mineralization. Their high Ca concentration allows the recording of Ca maps by using the negative secondary ion $CaO^-$ in the same sequence as the protein compositional negative secondary ion $CN^-$ or $S^-$. Iron is also present in the AmD in agreement with "in vivo" RMI observations and "in vitro" histochemical Perl staining of so called "thalamic spots" (Dhenain et al., Characterization of in vivo MRI detectable thalamic plaques from APP/PS1 mice, manuscript in preparation; El Tannir El Tayara et al., 2006; Vanhoutte et al., 2005). In the higher mineralized AmD, the "aggregates," no significant amount of iron was detected neither by nanoSIMS nor by X-ray analysis.

Although the contrast that can be observed in the SIMS images indicates the elemental distribution, quantification of SIMS images is not straightforward. The absolute element concentration cannot be deduced directly from the measured ion signals. Generally speaking, the conversion from ion intensity to concentration relies on the signal normalization, which requires the use of relative sensitivity factors calibrated from a reference sample that has a known composition, under the same measurement conditions. Several factors may influence the secondary ion emission and two main problems have to be taken into account:

1. The stability of the ion emission. During primary ion bombardment, the intensity of secondary ions increases due to the enhanced ionization yield, itself a result of the incorporation of primary species onto the surface of the sample. A steady state of emission is reached only after primary ion implantation with a certain dose, which may vary from one biological tissue to another even if their composition is quite similar. It is important for such a stable state to be attained for all the materials involved (Guerquin-Kern et al., 2005).
2. The dependence of the ion emission on the chemical environment (the so-called "matrix effects"). The matrix effects express the fact that the effective yield—the number of measured emitted ions by total ejected species (positive, negative, and neutral species)—can vary significantly for a given element depending on the chemical environment. Such dependence also changes from one element to another. Consequently, an element present in the same concentration in two different cellular compartments may exhibit differences in emission. In the case of trace elements, it is possible that these can be detected in one compartment but not detected in the other due solely to poor emission because a strong matrix effect. For this reason it is worth comparing the nanoSIMS results in the event of no detection with those obtained with other nanoprobe methods. We have performed this type of analysis on the higher mineralized aggregates and on the SPs where the iron was not detected by nanoSIMS. X-ray microanalysis of aggregates showed a very low iron content. TEM observations and nanoprobe X-ray analysis (Quintana et al., 2006) showed the presence of some Ft cores between the βA bundles in the coronal region of the SPs. In these cases, this means that the number of Iron atoms is insufficient to be detected by nanoSIMS and the failure to detect them is due to a low concentration rather than a strong matrix effect.

In the case of resin-embedded biological tissues, the matrix components C, H, and O have quite similar contents in resin and in tissue; consequently a similar "matrix effect" for the different cell compartments can be assumed. It should be possible to evaluate the concentration of minor elements such as Sulfur or Phosphorus directly by comparing the respective ion intensities. For pathological tissues to be analyzed, for example, healthy tissues present in the same section would be used as the reference sample to evaluate the concentration of compositional elements such as Sulfur bound to proteins. On the basis of the data obtained on condensed chromatin of glial cell nuclei (Fig. 3) with $S^-$ signal at 200 counts for an evaluated concentration of 162 ppm (Von Zglinicki et al., 1987), the S concentration in other different protein-containing regions, simultaneously mapped, can be evaluated: S concentration in the middle of SPs is found to be 219 ppm (271 mean counts) and 300 ppm (370 mean counts) in the nucleole of a damaged neighboring neuron. In the S-rich granular region near to SPs, two regions of different intensity of emission can be observed and the S concentrations have been evaluated at 563 and 796 ppm (695 and 983 mean counts, respectively).

In the absence of an internal standard, quantification of $Ca^+$ SIMS maps of the aggregates in transgenic mice was not possible but the complementary semiquantitative X-ray microanalysis shows a higher Ca/S ratio when compared with the partially mineralized AmD that indicate an increase of the mineralized phase in the aggregates. Furthermore $Fe^+$ emission in AmD is lower than that found in blood vessels containing erythrocytes found near the AmD [Fe concentration in cryosections of erythrocytes was evaluated by X-ray analysis as 52 ± 3 mM/kg dry weight by (Leapman and Ornberg, 1988) and as 19 ± 2 mM/kg dry weight by (Zierold et al., 1991), equivalent to 153 ppm At and 56 ppm At, respectively in embedded cells]. X-Ray semiquantitative analysis on erythrocytes and AmD (Table 1) confirms that the Fe/S concentration in the AmD is about 40% lower than in erythrocytes, showing, at least in this system and for semiquantitative purposes, the absence of a notable matrix effect between the $Fe^+$ emission in erythrocytes and the one in the AmD.

In the present work, we have used the conventional TEM method for the preparation of biological tissues i.e., chemical fixation, alcohol dehydration, and high-temperature resin embedding. These conventional methods are suitable for compositional biological elements such as Nitrogen, Phosphorous, and Sulfur and for Iron stoked in macromolecules such as Ft and Hm but not for diffusible elements such as Calcium in cells. The observed Ca accumulation in cell nuclei is the result of the artifactual relocation of this element during the preparative process.

Finally, it has recently been reported that synchrotron-based techniques, X-ray fluorescence and X-ray absorption near edge spectroscopy (XANES), have been used for “in situ” detection, identification, and mapping of small-scale iron components in the brain. (Mikhaylova et al., 2005). XANES has a good sensitivity, better than 1 ppm, and submicron resolution can be obtained in optimal experimental conditions. Nevertheless, the maps cannot be easily correlated with cell and tissue structures. The technique has recently been applied, with a spatial resolution of about 5 μm, to the study of metal compounds in pigeon brains and human AD brains (Collingwood et al., 2005a,b; Mikhaylova et al., 2005). It might be interesting to perform parallel studies, on the same samples, with nanoSIMS and XANES, to determine the valence state of the Iron in the pathological Ft observed in human brain (Quintana et al., 2000, 2004).

## CONCLUSION

Reported results in this study have pointed out that elemental analysis carried out using microprobe approaches in well-characterized brain regions may provide new finding for understanding the pathological processes associated to neurodegenation.

In addition, our observations on the hippocampus of AD patients and on the thalamus of transgenic APP/PS1 mice, allow us to establish that the NanoSIMS-50 Ion microscope (a dynamic SIMS nanoprobe) is a highly useful instrument for imaging the morphological and chemical modifications that take place in well-characterized pathological brain regions. Applied to the human brain, our results show, at the subcellular level, the pathological iron–ferritin–hemosiderin distribution in the hippocampus of AD patients. Applied to transgenic mice brain, our results have shown the presence of calcium-iron mineralization in thalamus AmD observed as hypointense spots in “in vivo” and “in vitro” RM images.

## ACKNOWLEDGMENTS

The authors express their gratitude to Drs. J.P. Haw, C. Duyckaerts, and V. Sazdovitch of Pitié-Salpetrière Brain Bank, Raymond Escourolle Neuropathology Department Paris, France. They thank all the members of the U350-INSERM-Institut Curie-Recherche-Orsay for the warm reception during the sabbatical stay of CQ at the nanoSIMS facility. Partially conventional TEM studies were supported by the CSNSM IN2P3-Orsay Center. The authors are grateful to Odile Kaitasov for helpful assistance and also thank J. Degrouard, D. Jaillard, C. Patiño, and R. Arranz for their technical assistance.

## REFERENCES

Andrási E, Igaz S, Szoboszlai N, Frakas E, Ajtony Z. 1999. Several methods to determine heavy metals in the human brain. Spectrochim Acta Part B 54:819–825.

Blanchard V, Moussaoui S, Czech C, Touchet N, Bonici B, Planche M, Canton T, Jedidi I, Gohin M, Wirths O, Bayer TA, Langui D, Duyckaerts C, Tremp G, Pradier L. 2003. Time sequence of maturation of dystrophic neurites associated with Ab deposits in APP/PS1 transgenic mice. Exp Neurol 184:247–263.

Connor JR, Menzies SL. 1995. Cellular management of iron in the brain. J Neurol Sci 134(Suppl):33–44.

Collingwood JF, Mikhaylova A, Davidson MR, Batich C, Streit WJ, Eskin T, Terry J, Barrea R, Underhill RS, Dobson J. 2005a. High-resolution X-ray absorption spectroscopy studies of metal compounds in neurodegenerative brain tissue. J Phys: Conf Ser 17:54–60.

Collingwood JF, Mikhaylova A, Davidson MR, Batich C, Streit WJ, Terry J, Dobson J. 2005b. In situ characterization and mapping of iron compounds in Alzheimer’s disease tissue. J Alzheimers Dis 7:267–272.

El Tannir El Tayara N, Delatour B, Le Cudennec C, Guegan M, Volk A, Dhenain M. 2006. Age-related evolution of amyloid burden, iron load, and MR relaxation times in a transgenic mouse model of Alzheimer’s disease. Neurobiol Dis 22:199–208.

Good PF, Perl DP, Bierer L, Schmeidler J. 1992a. Selective accumulation of aluminium and iron in the neurofibrillary tangled of Alzheimer’s disease: A laser microsprobe (LAMMA) study. Ann Neurol 31:286–292.

Good PF, Olanow CW, Perl DP. 1992b. Neuromelanin-containing neurons of the substantia nigra acumulate iron and aluminum in Parkinson’s disease: A LAMMA study. Brain Res 593:343–346.

Griffiths PD, Dobson BR, Jones GR, Clarke DT. 1999. Iron in the basal ganglia in Parkinson’s disease. An in vitro study using extended X-ray absorption fine structure and cryo-electron microscopy. Brain 122:667–673.

Grundke-Iqbal I, Fleming J, Tung YC, Lassmann H, Iqbal K, Joshi JG. 1990. Ferritin is a component of the neuritic (senile) plaque in Alzheimer dementia. Acta Neuropathol 81:105–110.

Guerquin-Kern JL, Wu TD, Quintana C, Croisy A. 2005. Progress in analytical imaging of the cell by dynamic secondary ion mass spectrometry (SIMS microscopy). Biochim Biophys Acta 1724:228–238.

Hirsch EC, Brandel JP, Galle P, Javoy-Agid F, Agid Y. 1991. Iron and Aluminum increase in the substantia nigra of patients with Parkinson’s disease: An X-ray microanalysis. J Neurochem 56:446–451.

Jellinger K, Kienzl E, Rumpelmair G, Riederer P, Stachelberger H, Ben-Shachar D, Youdim MBH. 1992. Iron-melanin complex in substantia nigra of Parkinsonian brains: An X-Ray microanalysis. J Neurochem 59:1168–1171.

Ke Y, Qian ZM. 2003. Iron misregulation in the brain: A primary cause of neurodegenerative disorders. Lancet Neurol 2:246–253.

Leapman RD, Ornberg RL. 1988. Quantitative electron energy loss spectroscopy in Biology. Ultramicroscopy 24:251–268.

Mikhaylova A, Davidson MR, Toastman H, Channell JET, Guyodo Y, Batich C, Dobson J. 2005. Detection, identification and mapping of iron anomalies in brain tissue using X-ray absorption spectroscopy. J Royal Soc Interface 2:33–37.

Nguyen-Legros J, Bizot J, Bolesse M, Pulicani JP. 1980. "Diaminobenzidine black": A new histochemical method for the visualization of exogenous iron. Histochemistry 66:239–244.

Perl DP, Good BS. 1992. Comparative techniques for determining cellular iron distribution in brain tissues. Ann Neurol 32:S76–S81.

Puchtler H, Sweat F, Levine M. 1962. On the binding of Congo red by amyloid. J Histochem Cytochem 10:355–364.

Quintana C, Lancin M, Marhic C, Pérez M, Martin-Benito J, Avila J, Lopez-Carrascosa JL. 2000. Initial studies with high resolution tem and electron energy loss spectroscopy studies of ferritin cores extracted from brains of patients with progressive supranuclear palsy and Alzheimer disease. Cell Mol Biol 46:807–820.

Quintana C, Cowley JM, Marhic C. 2004. Electron diffraction and high-resolution electron microscopy studies of the structure and composition of physiological and pathological ferritin. J Struct Biol 147:166–178.

Quintana C, Bellefqih S, Laval JY, Guerquin-Kern JL, Wu TD, Avila J, Ferrer I, Arranz R, Patiño C. 2006. Study of the localization of iron, ferritin and hemosiderin in Alzheimer's disease hippocampus by analytical microscopy at the subcellular level. J Struct Biol 153:42–54.

Rajan MT, Jagannatha Rao KS, Mamatha BM, Rao RV, Shanmugavelu P, Menon RB, Pavithran MV. 1997. Quantification of trace elements in normal brain by inductively coupled plasma atomic emission spectrometry. J Neurol Sci 146:153–166.

Rasband ,WS. 1997–2006. ImageJ. U.S. National Institutes of Health: Bethesda, MD. Available at http://rsb.info.nih.gov/ij/.

Slodzian G, Daigne B, Girard F, Boust F, Hillion F. 1992a. Scanning secondary ion analytical microscopy with parallel detection. Biol Cell 74:43–50.

Slodzian G, Daigne B, Girard F. 1992b. From direct ion images to ion probe scanning. Microsc Microanal Microstruct 3:99–118.

Smith MA, Harris PLR, Sayre LM, Perry G. 1997. Iron accumulation in AD is a source of redox-generated free radicals. Proc Natl Acad Sci USA 94:9866–9868.

Suvorova EI, Buffat PA. 2001. Electron diffraction and high resolution transmission electron microscopy in the characterization of calcium phosphate precipitation from aqueous solution under biomineralization conditions. Eur Cell Mater 1:27–42.

Todorich BM, Connor JR. 2004. Redox metals in Alzheimer's disease. Ann NY Acad Sci 1012:171–178.

Vanhoutte G, Dewachter I, Borghgraef P, Van Leuven F, Van der Linden A. 2005. Noninvasive in vivo MRI detection of neuritic plaques associated with iron in APP[V717I] transgenic mice, a model for Alzheimer's disease. Magn Reson Med 53:607–613.

Von Zglinicki T, Bimmler M. 1987. The intracellular distribution of ions and water in rat liver and heart muscle. J Microsc 146:77–85.

Wirths O, Multhaup G, Czech C, Blanchard V, Moussaoui S, Tremp G, Pradier L, Beyreuther K, Bayer TA. 2001a. Intraneuronal Abeta accumulation precedes plaque formation in β-amyloid precursor protein and presenilin-1 double-transgenic mice. Neurosci Lett 306:116–120.

Wirths O, Multhaup G, Czech C, Blanchard V, Tremp G, Pradier L, Beyreuther K, Bayer TA. 2001b. Reelin in plaques of β-amyloid precursor protein and presenilin-1 double-transgenic mice. Neurosci Lett 316:145–148.

Young D, Wilmer JP, Kisilevsky R. 1989. The ultrastructural localization of sulfated proteoglycans is identical in the amyloids of Alzheimer's disease, senile cardiac and medullary carcinoma-associated amyloidosis. Acta Neuropathol 78:202–209.

Zierold K, Tobler M, Müller M. 1991. X-ray microanalysis of high-pressure and impact frozed erythrocytes. J Microsc 161:RP1–RP2.